

***Euclid*: Finding strong gravitational lenses in the Early Release Observations using convolutional neural networks[★]**

B. C. Nagam^{★1,2}, J. A. Acevedo Barroso³, J. Wilde⁴, I. T. Andika^{5,6}, A. Manjón-García⁷, R. Pearce-Casey⁸, D. Stern⁹, J. W. Nightingale¹⁰, L. A. Moustakas⁹, K. McCarthy⁹, E. Moravec¹¹, L. Leuzzi^{12,13}, K. Rojas¹⁴, S. Serjeant⁸, T. E. Collett¹⁵, P. Matavulj¹⁴, M. Walmsley^{16,17}, B. Clément^{3,18}, C. Tortora¹⁹, R. Gavazzi^{20,21}, R. B. Metcalf^{12,13}, C. M. O’Riordan⁶, G. Verdoes Kleijn¹, L. V. E. Koopmans¹, E. A. Valentijn¹, V. Busillo^{19,22,23}, S. Schuldt^{24,25}, F. Courbin^{4,26}, G. Varnardos^{27,28}, M. Meneghetti^{13,29}, A. Díaz-Sánchez⁷, J. M. Diego³⁰, L. R. Ecker^{31,32}, T. T. Thai^{20,33}, A. R. Cooray³⁴, H. M. Courtois³⁵, L. Delchambre³⁶, G. Despali^{12,13,29}, D. Sluse³⁶, L. Ulivi^{37,38,39}, A. Melo^{6,5}, P. Corcho-Caballero¹, B. Altieri⁴⁰, A. Amara⁴¹, S. Andreon⁴², N. Auricchio¹³, H. Aussel⁴³, C. Baccigalupi^{44,45,46,47}, M. Baldi^{48,13,29}, A. Balestra⁴⁹, S. Bardelli¹³, P. Battaglia¹³, D. Bonino⁵⁰, E. Branchini^{51,52,42}, M. Brescia^{22,19}, J. Brinchmann^{53,54}, A. Caillat²⁰, S. Camera^{55,56,50}, V. Capobianco⁵⁰, C. Carbone²⁵, J. Carretero^{57,58}, S. Casas⁵⁹, M. Castellano⁶⁰, G. Castignani¹³, S. Cavuoti^{19,23}, A. Cimatti⁶¹, C. Colodro-Conde⁶², G. Congedo⁶³, C. J. Conselice¹⁷, L. Conversi^{64,40}, Y. Copin⁶⁵, M. Cropper⁶⁶, A. Da Silva^{67,68}, H. Degaudenzi⁶⁹, G. De Lucia⁴⁵, A. M. Di Giorgio⁷⁰, J. Dinis^{67,68}, F. Dubath⁶⁹, C. A. J. Duncan¹⁷, X. Dupac⁴⁰, S. Dusini⁷¹, M. Fabricius^{32,31}, M. Farina⁷⁰, S. Farrens⁴³, S. Ferriol⁶⁵, M. Frailis⁴⁵, E. Franceschi¹³, M. Fumana²⁵, K. George³¹, W. Gillard⁷², B. Gillis⁶³, C. Giocoli^{13,29}, P. Gómez-Alvarez^{73,40}, A. Grazian⁴⁹, F. Grupp^{32,31}, L. Guzzo^{24,42}, S. V. H. Haugan⁷⁴, J. Hoar⁴⁰, W. Holmes⁹, I. Hook⁷⁵, F. Hormuth⁷⁶, A. Hornstrup^{77,78}, P. Hudelot²¹, K. Jahnke⁷⁹, M. Jhabvala⁸⁰, B. Joachimi⁸¹, E. Keihänen⁸², S. Kermiche⁷², B. Kubik⁶⁵, K. Kuijken⁸³, M. Kümmel³¹, M. Kunz⁸⁴, H. Kurki-Suonio^{85,86}, R. Laureijs^{87,1}, D. Le Mignant²⁰, S. Ligi⁵⁰, P. B. Lilje⁷⁴, V. Lindholm^{85,86}, I. Lloro⁸⁸, G. Mainetti⁸⁹, E. Maiorano¹³, O. Mansutti⁴⁵, O. Marggraf⁹⁰, K. Markovic⁹, M. Martinelli^{60,91}, N. Martinet²⁰, F. Marulli^{12,13,29}, R. Massey⁹², E. Medinaceli¹³, M. Melchior¹⁴, Y. Mellier^{93,21}, E. Merlin⁶⁰, G. Meylan³, M. Moresco^{12,13}, L. Moscardini^{12,13,29}, R. Nakajima⁹⁰, C. Neissner^{94,58}, R. C. Nichol⁴¹, S.-M. Niemi⁸⁷, C. Padilla⁹⁴, S. Paltani⁶⁹, F. Pasian⁴⁵, K. Pedersen⁹⁵, W. J. Percival^{96,97,98}, V. Pettorino⁸⁷, S. Pires⁴³, G. Polenta⁹⁹, M. Poncet¹⁰⁰, L. A. Popa¹⁰¹, L. Pozzetti¹³, F. Raison³², R. Rebolo^{62,102,103}, A. Renzi^{104,71}, J. Rhodes⁹, G. Riccio¹⁹, E. Romelli⁴⁵, M. Roncarelli¹³, E. Rossetti⁴⁸, R. Saglia^{31,32}, Z. Sakr^{105,106,107}, A. G. Sánchez³², D. Sapone¹⁰⁸, B. Sartoris^{31,45}, M. Schirmer⁷⁹, P. Schneider⁹⁰, T. Schrabback¹⁰⁹, A. Secroun⁷², G. Seidel⁷⁹, S. Serrano^{110,111,112}, C. Sirignano^{104,71}, G. Sirri²⁹, J. Skottfelt¹¹³, L. Stanco⁷¹, J.-L. Starck⁴³, J. Steinwagner³², P. Tallada-Crespí^{57,58}, D. Tavagnacco⁴⁵, A. N. Taylor⁶³, H. I. Teplitz¹¹⁴, I. Tereno^{67,115}, R. Toledo-Moreo¹¹⁶, F. Torradeflot^{58,57}, A. Tsyganov¹¹⁷, I. Tutusaus¹⁰⁶, L. Valenziano^{13,118}, T. Vassallo^{31,45}, A. Veropalumbo^{42,52,51}, Y. Wang¹¹⁴, J. Weller^{31,32}, A. Zacchei^{45,44}, E. Zucca¹³, C. Burigana^{119,118}, A. Mora¹²⁰, M. Pöntinen⁸⁵, and V. Scottéz^{93,121}

(Affiliations can be found after the references)

February 17, 2025

ABSTRACT

The Early Release Observations (ERO) from *Euclid* have detected several new galaxy-galaxy strong gravitational lenses, with the all-sky survey expected to find 170 000 new systems, greatly enhancing studies of dark matter, dark energy, and constraints on the cosmological parameters. As a first step, visual inspection of all galaxies in one of the ERO fields (Perseus) was carried out to identify candidate strong lensing systems and compared to the predictions from Convolutional Neural Networks (CNNs). However, the entire ERO data set is too large for expert visual inspection. In this paper, we therefore extend the CNN analysis to the whole ERO data set, using different CNN architectures and methodologies. Using five CNN architectures, we identified 8,469 strong gravitational lens candidates from I_E -band cutouts of 13 *Euclid* ERO fields, narrowing them to 97 through visual inspection, including 14 grade A and 31 grade B candidates. We present the spectroscopic confirmation of a strong gravitational lensing candidate, EUCL J081705.61+702348.8. The foreground lensing galaxy, an early-type system at $z = 0.335$, and the background source, a star-forming galaxy at $z = 1.475$ with [O II] emission, are both identified. Lens modelling using the *Euclid* strong lens modelling pipeline reveals two distinct arcs in a lensing configuration, with an Einstein radius of $1''.18 \pm 0''.03$, confirming the lensing nature of the system. These findings highlight the importance of a broad CNN search to efficiently reduce candidates, followed by visual inspection to eliminate false positives and achieve a high-purity sample of strong lenses in *Euclid*.

Key words. Gravitational lensing: strong; Methods: statistical; Surveys; Cosmology: observations; Techniques: image processing

1. Introduction

The deflection of light rays from a distant background source by a massive foreground object, a phenomenon known as strong gravitational lensing, produces multiple resolved images, arcs, or Einstein rings, depending upon relative positions and alignment of the source, lens, and observer. Strong lensing has many important applications, such as (i) mapping the mass distribution of galaxy (Broadhurst et al. 1995; Limousin et al. 2005; Koopmans 2004; Nightingale et al. 2019; Turyshev & Toth 2022), (ii) providing constraints on dark energy (Sarbu et al. 2001; Sereno 2002; Meneghetti et al. 2005; Biesiada 2006; Oguri et al. 2008; Shiralilou et al. 2020) and dark matter (Tortora et al. 2010; Gilman et al. 2019; Nadler et al. 2021; Vegetti et al. 2024), (iii) constraining the slope of inner mass density profile (e.g., Treu & Koopmans 2002; Zhang 2004; Gavazzi et al. 2007; Koopmans et al. 2009; Zitrin et al. 2012; Spiniello et al. 2015; Li et al. 2018; He et al. 2020; Şengül & Dvorkin 2022), and, (iv) measurement of the Hubble constant (H_0) using time-delay cosmography between multiple imaged sources (Rhee 1991; Kochanek 2003; Grillo et al. 2018; Treu et al. 2022; Shajib et al. 2023; Birrer et al. 2024).

Gravitational lensing is sensitive to the presence of all foreground matter, regardless of whether this matter is in the form of visible baryonic matter or dark matter. To a very good approximation, dark matter appears to be collisionless, and lacking in detectable signatures of interactions via any of the fundamental forces except gravity. As such, gravitational lensing is one of the few probes of the dynamics and physical properties of dark matter particles that drive the growth of large-scale structures in the Universe and dominate the cosmic matter budget.

The *Euclid* mission (Euclid Collaboration: Mellier et al. 2024) is a 1.2 m space survey telescope with primary science objectives including measurements of cosmic shear from weak lensing, and galaxy clustering, from which cosmological parameter constraints follow. *Euclid* was successfully launched in July 2023 and is in the process of observing approximately one-third of the sky in its wide survey (Euclid Collaboration: Scaramella et al. 2022), and $\sim 50 \text{ deg}^2$ in its deep fields, about two magnitudes deeper than the wide survey. *Euclid*'s instruments consist of a visible imager (VIS), a near-infrared imager and a slitless spectrometer (NIS), and are described in more detail in Euclid Collaboration: Cropper et al. (2024) and Euclid Collaboration: Jahnke et al. (2024), respectively. The vast imaging and spectroscopic dataset from the *Euclid* survey enables a wide range of legacy science. Data sets such as these generally excel in their potential for discovering rare objects.

Euclid is widely expected to be transformative in the field of strong gravitational lensing, with 170 000 galaxy-scale strong lenses predicted in its wide survey (e.g., Collett 2015), increasing the number of known strong lenses by about two orders of magnitude. This creates a new frontier of rare object discovery, such as the detection of highly magnified high-redshift (e.g., $z > 2$) background sources, or of ‘‘Jackpot’’ systems with two background galaxies magnified at different redshifts being magnified by the same foreground lens. Each of these opens the possibility of a range of new legacy science goals for *Euclid*, including the direct detection and statistical characterization of dark matter halo substructure (e.g., Vegetti & Vogelsberger 2014; Hezaveh et al. 2016; Li et al. 2016, 2017; Despali et al. 2018; O’Riordan et al. 2023), geometrical constraints on the dark energy equation of state (e.g., Gavazzi et al. 2008; Stern et al. 2010;

Shlivko & Steinhardt 2024), and calibration of initial mass function of early-type galaxies (Treu et al. 2010; Barnabè et al. 2013; Leier et al. 2016).

However, identifying these $\sim 10^5$ strong lensing systems among the $\sim 10^9$ *Euclid* galaxies is a non-trivial task. Driven by *Euclid* and other major sky surveys, many authors have developed machine learning methods for finding strong gravitational lensing systems (e.g., Petrillo et al. 2017, 2019a,b; Lanusse et al. 2018; Pourrahmani et al. 2018; Schaefer et al. 2018; Davies et al. 2019; Metcalf et al. 2019; Li et al. 2020, 2021; Christ et al. 2020; Cañameras et al. 2020; Christ et al. 2020; Huang et al. 2017; Rezaei et al. 2022; Andika et al. 2023; Gentile et al. 2021; Savary et al. 2022; Rojas et al. 2022; Wilde et al. 2022; Nagam et al. 2023, 2024).

The first data released from *Euclid* were the Early Release Observations (ERO) (Cuillandre et al. 2024; Martín et al. 2024; Massari et al. 2024; Hunt et al. 2024; Saifollahi et al. 2024; Cuillandre et al. 2024; Marleau et al. 2024; Kluge et al. 2024; Atek et al. 2024; Weaver et al. 2024). As a first test for the existence of a large population of strong gravitational lenses, Acevedo Barroso et al. (2024, hereafter AB24) inspected all galaxies in the Perseus ERO field (Cuillandre et al. 2024), finding three gravitational lensing systems (termed grade A candidates), 13 probable systems (grade B candidates), and 52 possible strong lenses (grade C candidates). These were compared to the results of 21 CNN architectures in Pearce-Casey et al. (2024, hereafter PC24), with the result that, at best, CNNs produce lens candidate lists that are only $\sim 10\%$ pure. The best performing CNN was also one of the deepest networks, pre-trained on over a hundred million galaxy classifications from the Galaxy Zoo citizen science project (Lintott et al. 2008), with a final layer fine-tuned by re-training on strong lenses painted onto real galaxy images from the *Euclid* ERO data sets. However, some similarities were observed in the false positives, such as the presence of spiral arms in the target galaxy, suggesting that further improvements to the CNN architecture or training process are possible.

The entire *Euclid* ERO data set is too large for expert volunteers to conduct such an examination of every galaxy in a timely fashion. Therefore, in this paper, we present the results of our strong gravitational lens search in the remainder of the *Euclid* ERO data, using a CNN-based approach followed by visual inspection. In performing this analysis, we take an approach inspired by previous works (Jacobs et al. 2017, 2019; Andika et al. 2023; Nagam et al. 2023), by comparing the outputs of various CNN lens finders. Inevitably, the vast majority of *Euclid*'s strong gravitational lenses will first be identified through an initial CNN search, followed by visual inspection. However, this CNN search inevitably misses some strong lensing systems, resulting in a population of false negatives. Here, we attempt to mitigate this by considering a diversity of CNN approaches, searching for systems that are detected by one CNN and not another. This approach is particularly important for discovering rare lensing configurations that will contribute to *Euclid*'s legacy science goals.

This paper is structured as follows. In Sect. 2, we summarise the *Euclid* ERO data characteristics and the processing applied to them for the detection of strong gravitational lenses with CNNs. Section 3 presents the methodology used. The results are presented in Sect. 4, and the results of recent spectroscopic follow-up are presented in Sect. 5. The summary and the conclusions are discussed in Sect. 6.

* This paper is published on behalf of the Euclid Consortium.

** e-mail: b.c.nagam@rug.nl

2. *Euclid* Early Release Observation data

The *Euclid* ERO data release covers 17 galactic and extragalactic fields. The objective was to acquire scientific observations for communication and early scientific results before the start of the nominal mission ([Euclid Early Release Observations 2024](#); [Cuillandre et al. 2024](#)).

In this work, we focus on all the ERO fields except for the Perseus cluster, which has already been mined for lenses in AB24 and PC24. All ERO fields are covered by both the VIS and NISP instruments. However, in Table B.1, we present only the VIS statistics for brevity. We refer the reader to [Cuillandre et al. \(2024\)](#) for a more complete overview.

Given the $O(10^6)$ sources in the whole ERO catalogues, we narrow our selection to extended sources brighter than 23 magnitudes in VIS I_e -band. This is in agreement with the selection used in AB24 and PC24. Thus, the selection corresponds to $MAG_AUTO < 23$ and $CLASS_STAR < 0.5$ in the VIS catalogues, for a total of 377 472 sources. This classification is conservative and includes a significant fraction of stars.

We create postage stamps for every selected source. Each stamp covers $9''9 \times 9''9$, corresponding to 99×99 pixels in VIS and 33×33 pixels in the NISP bands. The stamp size is kept large enough to include any galaxy-scale lensing effects, given that the typical Einstein radius is rarely larger than $3''$, but also small enough to keep only the relevant information, without contamination from nearby sources.

3. Methodology

3.1. Candidate selection

We employed the following CNN models: 4-Layer CNN ([Manjón-García 2021](#)), DenseLens ([Nagam et al. 2023](#)), Lens-CLR ([Andika et al. in prep.](#)), MRC-95 ([Wilde 2023](#)), and Naberrrie ([Wilde 2023](#)). For a detailed overview of these models and their application to the *Euclid* ERO Perseus field, see PC24. We applied each of these CNN models to the 377 472 extracted VIS cutouts, obtaining five scores per source. To mitigate the impact of noise in individual classifications, we clipped scores below 0.1 and computed the geometric mean as the final score. The arbitrary clipping step helps to prevent the removal of good candidates due to noisy classifications.

Each CNN model was trained on different data sets and used different architectures, thereby capturing a wide variety of lensing and non-lensing features (see PC24 for more details). This aggregating method allowed for a more robust and consistent identification of lens candidates. From the initial 16 ERO fields, three fields (Horsehead, IC 342, and NGC 6254) were excluded from our final analysis since they did not contain any viable candidates. The cutouts were then ranked based on the geometric mean values, and the top 650 cutouts from each of the remaining 13 fields were selected, resulting in a total of 8450 cutouts chosen by the CNNs for further inspection. We adopt the same approach as AB24 and PC24, utilizing both the VIS and NISP bands for visual inspection, because the human eye is good at detecting subtle colour variations ([Marshall et al. 2009](#)). However, we exclude the NISP cutouts from the CNN inference process to focus on a single band, which is effective at capturing morphological features ([Petrillo et al. 2019a](#)), while acknowledging that incorporating additional bands could provide additional information and may improve classification performance.

3.2. Visual inspection of candidates

During the visual analysis of the results of individual models, 19 additional notable candidates were identified and included in the selection. This brought the total number of candidates to 8469, which were then subjected to a first round of visual inspection by 12 experts, in which the experts rejected obvious non-lenses. The voting results from this stage of visual inspection are illustrated in Fig. 1, showing the distribution of votes each candidate received. Based on the voting, 183 candidates that received three or more votes were selected for further inspection.

However, during the subsequent analysis, 32 of these 183 candidates were identified as duplicates, which were removed from the sample. These duplicates arose from the VIS source catalogue itself containing multiple entries for the same physical source, with slight positional shifts within $1''$ between the duplicate entries. This left 151 unique candidates, which then underwent a second, more rigorous round of visual inspection. This stage involved 15 experts who graded each candidate based on the presence of lensing features, using a grading scheme (see AB24) that categorized the candidates into four grades: A, B, C, and X. In short, the grading scheme implies the following:

- Grade A represents definite lenses with clear lensing features;
- Grade B suggests the presence of lensing features, though confirmation requires additional data;
- Grade C indicates lensing features that could also be attributed to other physical phenomena;
- Grade X refers to objects that are definitively not lenses.

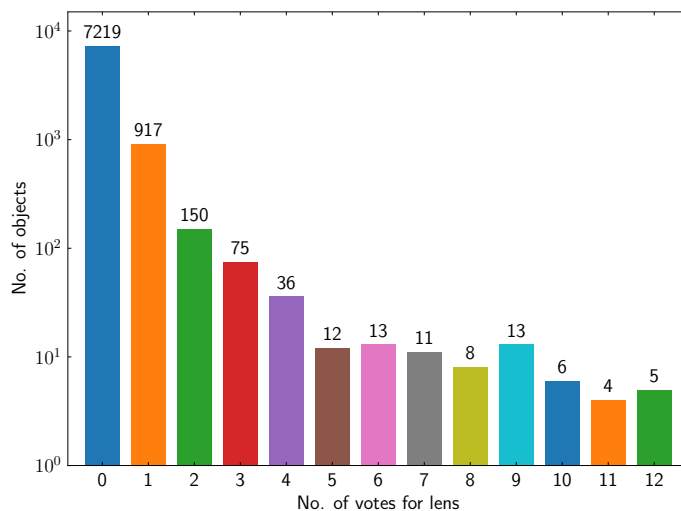


Fig. 1. The voting results for stage 1 of the visual inspection process, which involved 12 people, were based on 8469 candidates selected by CNNs.

4. Results

We present here an overview of the grade A, B, and C candidates found in our search of the ERO fields. Our search methodology combined multiple CNN models with visual classification to ensure robust candidate identification.

4.1. CNNs with visual classification

We identified a total of 97 lens candidates, distributed as 14 grade A candidates, 31 grade B candidates, and 52 grade C candidates with visual classification. We also identified 54 objects as

grade X (non-lenses) during our visual inspection process. The catalogue of all these candidates is shown in Table A.1.

The 14 grade A candidates, representing definite lenses, are shown in Fig. 2. The 31 grade B candidates, which exhibit strong lensing features but require further confirmation, are presented in Fig. 3. Due to the larger number of grade C candidates, we have divided their presentation across Figs. 4 and 5, collectively displaying all 52 grade C objects that show potential lensing characteristics but necessitate additional investigation.

4.2. Prediction

We compare our findings with predictions made by Collett (2015), who estimated that the *Euclid* mission would discover approximately 170 000 strong gravitational lenses over its planned survey area of 15 000 square degrees. Given that the 13 *Euclid* ERO fields we analysed cover a total area of 8.12 deg^2 , we would naively expect ~ 90 strong lenses in the ERO area, although this reduces to ~ 70 after applying our $I_E < 23$ pre-selection. Our study has identified 97 grade A, B, and C lens candidates, a number that aligns closely with the theoretical expectations. However, experience suggests that most grade C candidates are unlikely to be lenses. Taking Collett (2015) as truth and pessimistically assuming only our grade A candidates are lenses, we would conclude that our search is $\sim 15\%$ complete. If the grade B candidates are also all lenses we have found $\sim 60\%$ of all the lenses with $I_E < 23$ that are in the ERO fields.

5. Palomar spectroscopy

We obtained optical spectroscopic follow-up of several of the grade A and grade B candidates using the Double Spectrograph (DBSP; Oke & Gunn 1982) on the 5m Hale telescope at Palomar Observatory between June and October 2024. Table 1 presents the targets for which we were able to measure at least one redshift in the candidate strong lens system. All nights had typical $\sim 1''.2$ Palomar seeing. The June and July nights were photometric, while the October night had some clouds at the start, and end of the night, but was relatively clear at the time of the reported observation. For each observation, we obtained two or three exposures of 1200 s using the $1''.5$ slit, the 600 lines blue grating (blazed at 4000 \AA), the 5500 \AA dichroic, and the 316 lines red grating (blazed at 7500 \AA). The slits were aligned on the candidate lensing galaxy at a position angle to cover the putative lens feature. The data were reduced using standard techniques within the Image Reduction and Analysis Facility (IRAF).

All the lensing galaxies proved to be early-type galaxies with Ca H & K absorption and strong 4000 \AA breaks. One grade A system, EUCLJ081705.61+702348.8, revealed redshifts for both the foreground lensing galaxy and the background source galaxy, where the latter had a slightly ($\sim 1''.7$) offset emission line at 9222.8 \AA (Fig. 6). If the emission feature was associated with the primary target galaxy at $z = 0.335$, the implied rest-frame wavelength would be 6908 \AA , which does not correspond to any strong spectral features in galaxies, particularly early-type galaxies. Instead, the most plausible identification is [O II] emission from a lensed star-forming galaxy at $z = 1.475$.

To further confirm the lensing nature of EUCLJ081705.61+702348.8, we modelled the system using the *Euclid* strong lens modelling pipeline implemented in PyAutoLens (Nightingale et al. 2018, 2021). A full description of the pipeline and application to a larger sample of lenses will be provided in the Q1 data release papers (Rojas et al. 2025,

Walmsley et al. 2025). Figure 7 presents the results for the VIS optical image. The foreground lens galaxy light is subtracted by fitting it with a multi-Gaussian expansion composed of 60 Gaussians (He et al. 2024). This reveals two distinct arcs in locations that are consistent with a singular isothermal ellipsoid (SIE) mass model configuration. PyAutoLens fits the SIE lens model, which the right panel of Figure 7 shows accurately ray-traces both arcs to the same region of the source-plane. The source reconstruction reveals two separate doubly imaged emission components, which lie outside the tangential caustic but within the radial caustic, consistent with the tangential and radial critical curves predicted by our SIE mass model for this lens system. The SIE lens mass model includes an external shear, and the inferred Einstein radius is $1''.18 \pm 0''.03$.

6. Discussion and conclusions

We have presented a catalogue of strong gravitational lens candidates identified in the *Euclid* Early Release Observations, covering 13 fields with a total area of 8.12 deg^2 . Our search methodology, combining multiple CNN models with visual classification, has yielded 97 lens candidates: 14 grade A, 31 grade B, and 52 grade C candidates. This multi-stage approach, using CNNs for initial candidate selection followed by careful visual inspection, has proven effective in producing a high-purity sample, particularly for grade A and B candidates.

The spectroscopic follow-up of our highest-quality candidates, notably EUCLJ081705.61+702348.8, demonstrates the robustness of our classification system. Our spectroscopic analysis reveals an emission line at 9222.8 \AA that is most plausibly identified as [O II] from a lensed star-forming galaxy at $z = 1.475$, measuring the redshifts for both the foreground lensing galaxy ($z = 0.335$) and the background source galaxy. The lens model implemented in PyAutoLens fits the two distinct arcs, revealing a source reconstruction with two doubly imaged emission components located outside the tangential caustic but within the radial caustic, thus confirming the strong lensing configuration. The lens modelling measured an Einstein radius of $1''.18 \pm 0''.03$.

We compare our findings with theoretical predictions, indicating that the discovery of 97 candidates (across all grades) in 8.12 deg^2 is consistent with previous estimates of ~ 70 strong lenses in this area (after applying our $I_E < 23$ pre-selection). Taking a conservative approach where only grade A candidates are considered confirmed lenses, our search achieves $\sim 15\%$ completeness, rising to $\sim 60\%$ if grade B candidates are included. Our lower completeness rate compared to Zoobot1 (Walmsley et al. 2023), which identified 61 out of 68 known lenses (90% completeness) in RP24, may be attributed to the fact that in our study the true number of lenses is unknown, making it more challenging than studies where the ground truth was known. Furthermore, our selection of only the top 650 candidates based on geometric mean scores for each field, while chosen to maintain a reasonable balance between completeness and false positive rate, may have excluded some genuine lens candidates that received lower CNN scores.

This work serves as a guide for future *Euclid* lens searches, demonstrating that a broad initial CNN search followed by careful visual inspection is essential to build high-purity lens samples. Although our current analysis focuses on single-band (I_E) detections, the full potential of *Euclid* lens searches will be realized through multi-band analysis, refined CNN architectures, and expanded spectroscopic follow-up campaigns. The lens modelling pipeline demonstrated here for

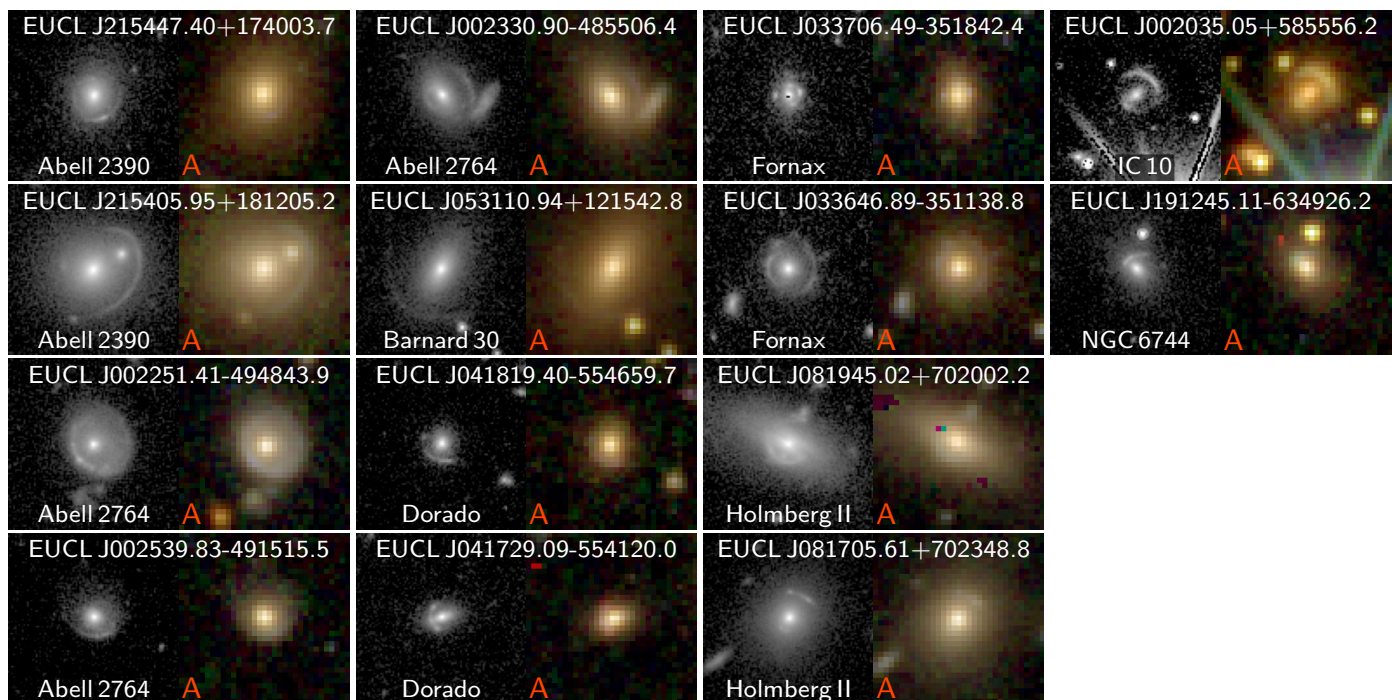


Fig. 2. Mosaic of the grade A lens candidates from the second round of visual inspection. For each candidate, we show the high-resolution I_E -band cutout on the left and the lower-resolution H_E , Y_E , I_E composite on the right. The IAU name and field name are displayed at the top and bottom of the I_E -band cutout, respectively, and the final joint grade is shown in red at the bottom of the composite cutout. Each cutout is $9'' \times 9''$ in size.

Table 1. Palomar spectroscopy of strong lens candidates.

IAU Name	Grade	Obs Date (UT)	PA (deg)	$z(\text{lens})$	$z(\text{source})$
EUCL J081705.61+702348.8	A	2024 Oct 03	-35	0.335	1.475
EUCL J215252.97+171932.8	B	2024 Jul 10	60	0.418	–
EUCL J215405.95+181205.2	A	2024 Jun 02	114	0.474	–
EUCL J215447.40+174003.7	A	2024 Oct 03	10	0.716	–

EUCL J081705.61+702348.8 provides a template for future systematic analysis of larger lens samples in upcoming *Euclid* data releases.

Acknowledgements. B.C.N. acknowledges support of DSSC and HPC cluster of RUG. J. A. A. B. and B. C. acknowledge support from the Swiss National Science Foundation (SNSF). C.T. acknowledges the INAF grant 2022 LEMON. A.M.G. acknowledges the support of project PID2022-141915NB-C22 funded by MCIU/AEI/10.13039/501100011033 and FEDER/UE. Based on observations obtained at the Hale Telescope, Palomar Observatory, as part of a collaborative agreement between the Caltech Optical Observatories and the Jet Propulsion Laboratory. This work made use of *Astropy*: a community-developed core Python package and an ecosystem of tools and resources for astronomy (*Astropy Collaboration et al. 2013, 2018, 2022*), *NumPy* (*Harris et al. 2020*), *Matplotlib* (*Hunter 2007*), and *pandas* (*McKinney et al. 2011*). This work has made use of the Early Release Observations (ERO) data from the *Euclid* mission of the European Space Agency (ESA), 2024, <https://doi.org/10.57780/esa-qmocze3>. The Euclid Consortium acknowledges the European Space Agency and a number of agencies and institutes that have supported the development of *Euclid*, in particular the Agenzia Spaziale Italiana, the Austrian Forschungsförderungsgesellschaft funded through BMK, the Belgian Science Policy, the Canadian Euclid Consortium, the Deutsches Zentrum für Luft- und Raumfahrt, the DTU Space and the Niels Bohr Institute in Denmark, the French Centre National d’Etudes Spatiales, the Fundação para a Ciência e a Tecnologia, the Hungarian Academy of Sciences, the Ministerio de Ciencia, Innovación y Universidades, the National Aeronautics and Space Administration, the National Astronomical Observatory of Japan, the Nederlandse Onderzoekschool Voor Astronomie, the Norwegian Space Agency, the Research Council of Finland, the Romanian Space Agency, the State Secretariat for Education, Research, and Innovation (SERI) at the Swiss Space Office (SSO), and the United King-

dom Space Agency. A complete and detailed list is available on the *Euclid* web site (www.euclid-ec.org).

References

- Acevedo Barroso, J. A., O’Riordan, C. M., Clément, B., et al. 2024, *A&A*, submitted, arXiv:2408.06217
- Andika, I. T., Suyu, S. H., Cañameras, R., et al. 2023, *A&A*, 678, A103
- Astropy* Collaboration, Price-Whelan, A. M., Lim, P. L., et al. 2022, *ApJ*, 935, 167
- Astropy* Collaboration, Price-Whelan, A. M., Sipőcz, B. M., et al. 2018, *AJ*, 156, 123
- Astropy* Collaboration, Robitaille, T. P., Tollerud, E. J., et al. 2013, *A&A*, 558, A33
- Atek, H., Gavazzi, R., Weaver, J., et al. 2024, *A&A*, accepted, arXiv:2405.13504
- Barnabè, M., Spiniello, C., Koopmans, L. V. E., et al. 2013, *MNRAS*, 436, 253
- Biesiada, M. 2006, *Phys. Rev. D*, 73, 023006
- Birrer, S., Millon, M., Sluse, D., et al. 2024, *Space Sci. Rev.*, 220, 48
- Broadhurst, T. J., Taylor, A. N., & Peacock, J. A. 1995, *ApJ*, 438, 49
- Cañameras, R., Schuldt, S., Suyu, S., et al. 2020, *A&A*, 644, A163
- Christ, C., Nord, B., Gozman, K., & Ottenbreit, K. 2020, in *AAS*, Vol. 235, 303–03
- Collett, T. E. 2015, *ApJ*, 811, 20
- Cropper, M., Pottinger, S., Niemi, S., et al. 2016, in *Space Telescopes and Instrumentation 2016: Optical, Infrared, and Millimeter Wave*, Vol. 9904, SPIE, 269–284
- Şengül, A. Ç. & Dvorkin, C. 2022, *MNRAS*, 516, 336
- Cuillandre, J.-C., Bertin, E., Bolzonella, M., et al. 2024, *A&A*, submitted, arXiv:2405.13496

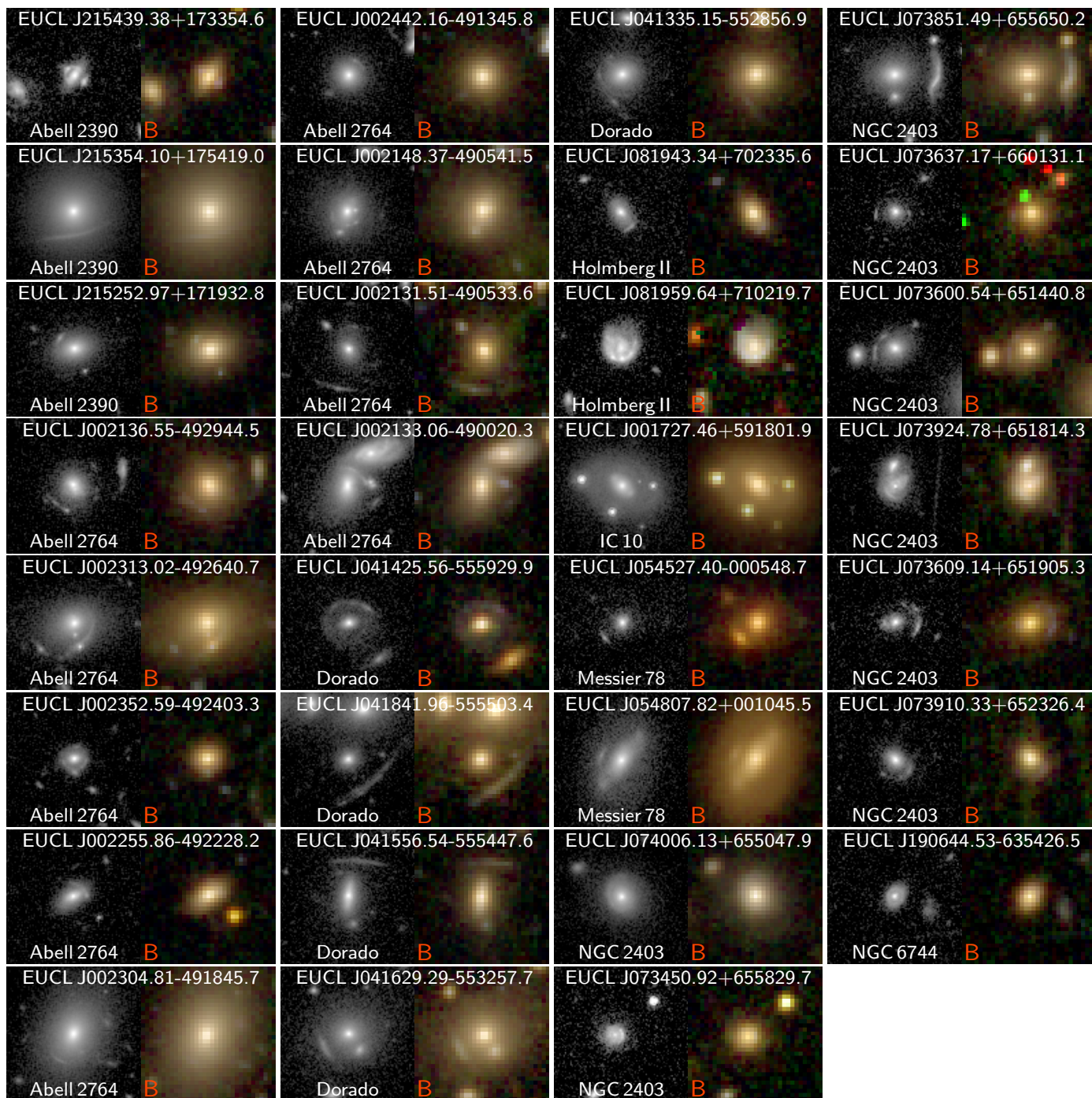


Fig. 3. Mosaic of the grade B lens candidates from the second round of visual inspection. For each candidate, we show the high-resolution I_e -band cutout on the left and the lower-resolution H_e , Y_e , I_e composite on the right. The IAU name and field name are displayed at the top and bottom of the I_e -band cutout, respectively, and the final joint grade is shown in red at the bottom of the composite cutout. Each cutout is $9'' \times 9''$ in size.

Cuillandre, J.-C., Bolzonella, M., Boselli, A., et al. 2024, arXiv preprint arXiv:2405.13501
 Cuillandre, J.-C., Bolzonella, M., Boselli, A., et al. 2024, A&A, submitted, arXiv:2405.13501
 Davies, A., Serjeant, S., & Bromley, J. M. 2019, MNRAS, 487, 5263
 Despali, G., Vegetti, S., White, S. D. M., Giocoli, C., & van den Bosch, F. C. 2018, MNRAS, 475, 5424
 Euclid Collaboration: Cropper, M., Al Bahlawan, A., Amiaux, J., et al. 2024, A&A, accepted, arXiv:2405.13492
 Euclid Collaboration: Jahnke, K., Gillard, W., Schirmer, M., et al. 2024, A&A, accepted, arXiv:2405.13493
 Euclid Collaboration: Mellier, Y., Abdurro'uf, Acevedo Barroso, J., et al. 2024, A&A, accepted, arXiv:2405.13491

Euclid Collaboration: Scaramella, R., Amiaux, J., Mellier, Y., et al. 2022, A&A, 662, A112
 Euclid Early Release Observations. 2024, <https://doi.org/10.57780/esa-qmocz3>
 Gavazzi, R., Treu, T., Koopmans, L. V. E., et al. 2008, ApJ, 677, 1046
 Gavazzi, R., Treu, T., Rhodes, J. D., et al. 2007, ApJ, 667, 176
 Gentile, F., Tortora, C., Covone, G., et al. 2021, MNRAS, 510, 500
 Gilman, D., Du, X., Benson, A., et al. 2019, MNRAS: Letters, 492, L12
 Grillo, C., Rosati, P., Suyu, S. H., et al. 2018, ApJ, 860, 94
 Harris, C. R., Millman, K. J., van der Walt, S. J., et al. 2020, Nature, 585, 357
 He, Q., Li, H., Li, R., et al. 2020, MNRAS, 496, 4717
 He, Q., Nightingale, J. W., Amvrosiadis, A., et al. 2024, MNRAS, 532, 2441
 Hezaveh, Y. D., Dalal, N., Marrone, D. P., et al. 2016, ApJ, 823, 37

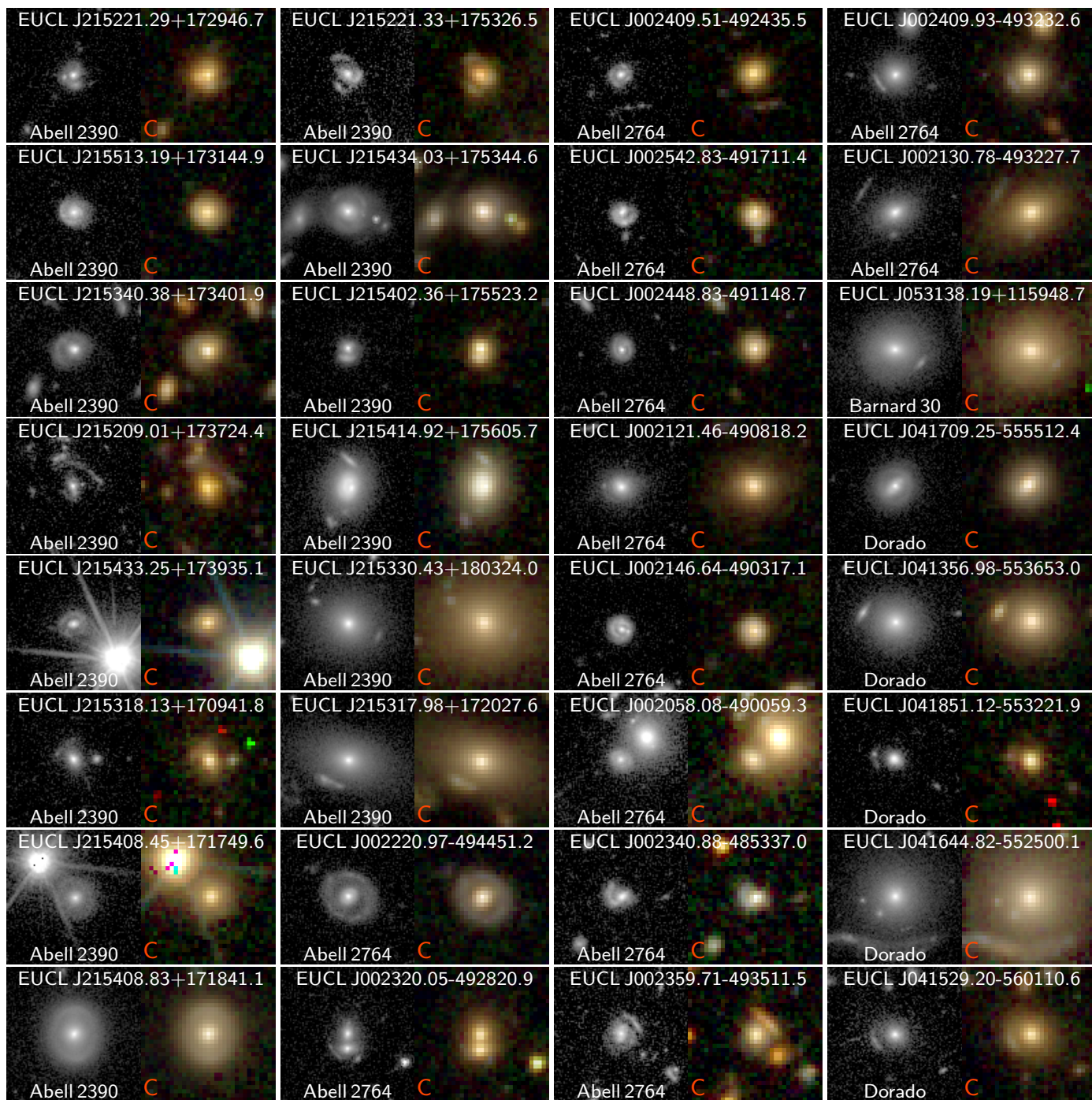


Fig. 4. Mosaic of the 32 out of 52 grade C lens candidates from the second round of visual inspection. For each candidate, we show the high-resolution I_E -band cutout on the left and the lower-resolution H_E , Y_E , I_E composite on the right. The IAU name and field name are displayed at the top and bottom of the I_E -band cutout, respectively, and the final joint grade is shown in red at the bottom of the composite cutout. Each cutout is $9'' \times 9'' \times 9''$ in size.

Huang, G., Liu, Z., Van Der Maaten, L., & Weinberger, K. Q. 2017, in CVPR, 4700–4708
 Hunt, L., Annibali, F., Cuillandre, J.-C., et al. 2024, A&A, accepted, arXiv:2405.13499
 Hunter, J. D. 2007, CiSE, 9, 90
 Jacobs, C., Collett, T., Glazebrook, K., et al. 2019, MNRAS, 484, 5330
 Jacobs, C., Glazebrook, K., Collett, T., More, A., & McCarthy, C. 2017, MNRAS, 471, 167
 Kluge, M., Hatch, N., Montes, M., et al. 2024, A&A, accepted, arXiv:2405.13503
 Kochanek, C.S., P. L. S. 2003, Carnegie Observatories Astrophysics Series, 2, 211
 Koopmans, L. V. E. 2004 [arXiv:astro-ph/0412596]

Koopmans, L. V. E., Bolton, A., Treu, T., et al. 2009, ApJ, 703, L51
 Lanusse, F., Ma, Q., Li, N., et al. 2018, MNRAS, 473, 3895
 Leier, D., Ferreras, I., Saha, P., et al. 2016, MNRAS, 459, 3677
 Li, R., Frenk, C. S., Cole, S., et al. 2016, MNRAS, 460, 363
 Li, R., Frenk, C. S., Cole, S., Wang, Q., & Gao, L. 2017, MNRAS, 468, 1426
 Li, R., Napolitano, N., Spiniello, C., et al. 2021, ApJ, 923, 16
 Li, R., Napolitano, N. R., Tortora, C., et al. 2020, ApJ, 899, 30
 Li, R., Shu, Y., & Wang, J. 2018, MNRAS, 480, 431
 Limousin, M., Kneib, J.-P., & Natarajan, P. 2005, MNRAS, 356, 309
 Lintott, C. J., Schawinski, K., Slosar, A., et al. 2008, MNRAS, 389, 1179
 Manjón-García, A. 2021, PhD thesis, University of Cantabria (Spain)
 Marleau, F., Cuillandre, J.-C., Cantiello, M., et al. 2024, A&A, accepted, arXiv:2405.13502

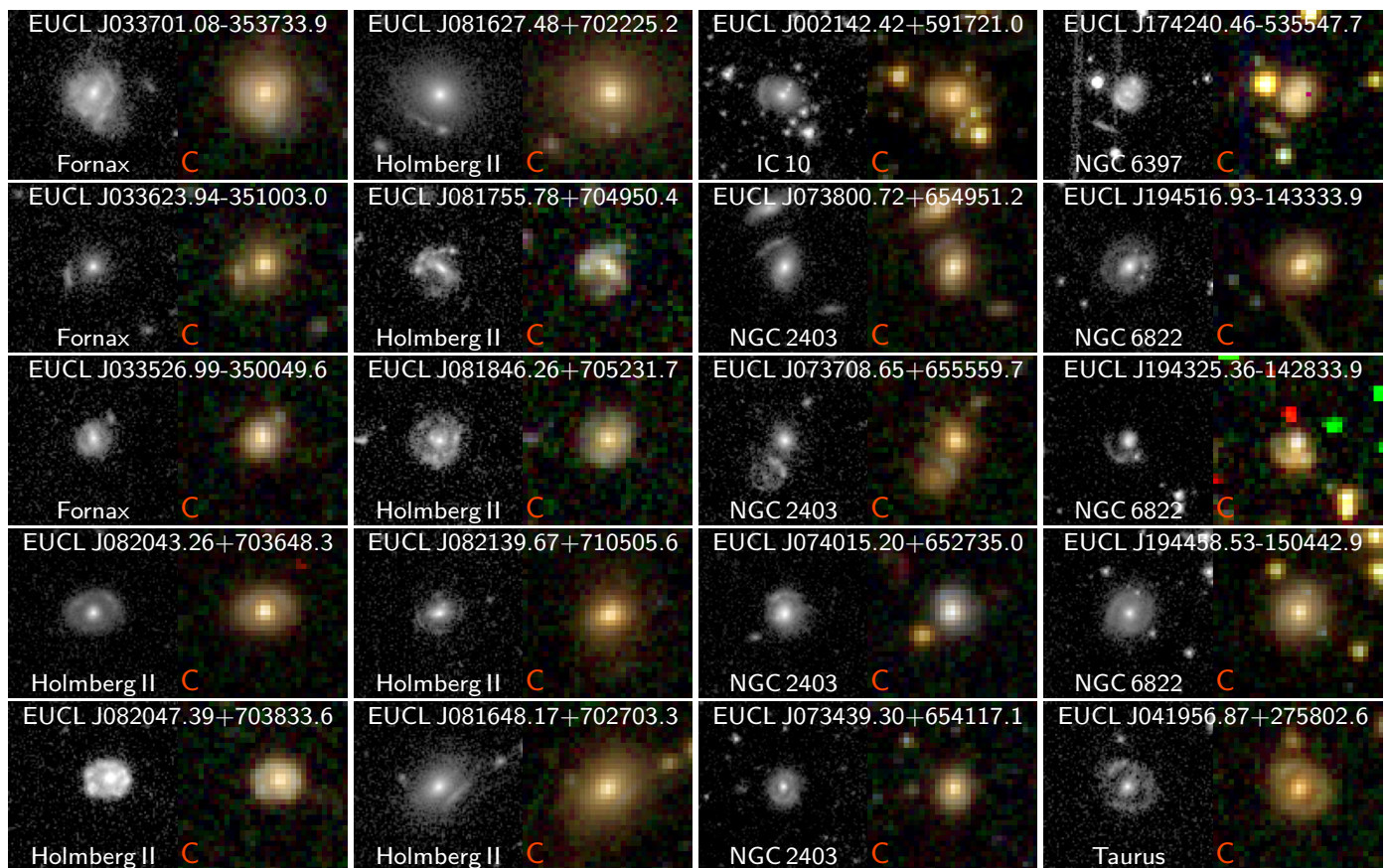


Fig. 5. Mosaic of the remaining 20 grade C lens candidates from the second round of visual inspection. For each candidate, we show the high-resolution I_E -band cutout on the left and the lower-resolution H_E , Y_E , I_E composite on the right. The IAU name and field name are displayed at the top and bottom of the I_E -band cutout, respectively, and the final joint grade is shown in red at the bottom of the composite cutout. Each cutout is $9'9 \times 9'9$ in size.

Marshall, P. J., Hogg, D. W., Moustakas, L. A., et al. 2009, *ApJL*, 694, 924
 Martín, E., Žerjal, M., Bouy, H., et al. 2024, *A&A*, accepted, arXiv:2405.13497
 Massari, D., Dalessandro, E., Erkal, D., et al. 2024, *A&A*, accepted, arXiv:2405.13498
 McKinney, W. et al. 2011, *PyHPC*, 14, 1
 Meneghetti, Bartelmann, M., Dolag, K., et al. 2005, *A&A*, 442, 413
 Metcalf, Meneghetti, M., Avestruz, C., et al. 2019, *A&A*, 625, A119
 Nadler, E. O., Birrer, S., Gilman, D., et al. 2021, *ApJ*, 917, 7
 Nagam, B. C., Koopmans, L. V. E., Valentijn, E. A., et al. 2023, *MNRAS*, 523, 4188
 Nagam, B. C., Koopmans, L. V. E., Valentijn, E. A., et al. 2024, *MNRAS*, 533, 1426
 Nightingale, J., Hayes, R., Kelly, A., et al. 2021, *J. Open Source Softw.*, 6, 2825
 Nightingale, J. W., Dye, S., & Massey, R. J. 2018, *MNRAS*, 478, 4738
 Nightingale, J. W., Massey, R. J., Harvey, D. R., et al. 2019, *MNRAS*, 489, 2049
 Oguri, M., Inada, N., Strauss, M. A., et al. 2008, *AJ*, 135, 512
 Oke, J. & Gunn, J. 1982, *PASP*, 94, 586
 O’Riordan, C. M., Despali, G., Vegetti, S., Lovell, M. R., & Moliné, Á. 2023, *MNRAS*, 521, 2342
 Pearce-Casey, Nagam, B.C., Clement, B., & Tortora, C. 2024, *A&A*, this edition
 Petrillo, C. E., Tortora, C., Chatterjee, S., et al. 2017, *MNRAS*, 472, 1129
 Petrillo, C. E., Tortora, C., Chatterjee, S., et al. 2019a, *MNRAS*, 482, 807
 Petrillo, C. E., Tortora, C., Vernardos, G., et al. 2019b, *MNRAS*, 484, 3879
 Pourrahmani, M., Nayyeri, H., & Cooray, A. 2018, *ApJ*, 856, 68
 Rezaei, S., McKean, J. P., Biehl, M., de Roo, W., & Lafontaine, A. 2022, *MNRAS*, 517, 1156
 Rhee, G. 1991, *Nature*, 350, 211
 Rojas, K., Savary, E., Clément, B., et al. 2022, *A&A*, 668, A73
 Saifollahi, T., Voggel, K., Lançon, A., et al. 2024, *A&A*, accepted, arXiv:2405.13500
 Sarbu, N., Rusin, D., & Ma, C.-P. 2001, *ApJ*, 561, L147
 Savary, E., Rojas, K., Maus, M., et al. 2022, *A&A*, 666, A1
 Schaefer, C., Geiger, M., Kuntzer, T., & Kneib, J.-P. 2018, *A&A*, 611, A2
 Sereno, 2002, *A&A*, 393, 757
 Shajib, A. J., Mozumdar, P., Chen, G. C.-F., et al. 2023, *A&A*, 673, A9

Shiralilou, B., Martinelli, M., Papadomanolakis, G., et al. 2020, *JCAP*, 04, 057
 Shlivko, D. & Steinhardt, P. J. 2024, *Physics Letters B*, 855, 138826
 Spiniello, C., Barnabè, M., Koopmans, L. V. E., & Trager, S. C. 2015, *MNRAS: Letters*, 452, L21
 Stern, D., Jimenez, R., Verde, L., Kamionkowski, M., & Stanford, S. A. 2010, *JCAP*, 02, 008
 Tortora, C., Napolitano, N. R., Romanowsky, A. J., & Jetzer, P. 2010, *ApJ*, 721, L1-L5
 Treu, T., Auger, M. W., Koopmans, L. V. E., et al. 2010, *ApJ*, 709, 1195
 Treu, T. & Koopmans, L. V. E. 2002, *ApJ*, 575, 87
 Treu, T., Suyu, S. H., & Marshall, P. J. 2022, *A&AR*, 30, 8
 Turyshev, S. G. & Toth, V. T. 2022, *MNRAS*, 513, 5355
 Vegetti, S., Birrer, S., Despali, G., et al. 2024, *Space Sci. Rev.*, 220, 58
 Vegetti, S. & Vogelsberger, M. 2014, *MNRAS*, 442, 3598
 Walmsley, M., Allen, C., Aussel, B., et al. 2023, *JOSS*, 8
 Weaver, J., Taamoli, S., McPartland, C., et al. 2024, *A&A*, accepted, arXiv:2405.13505
 Wilde, J., Serjeant, S., Bromley, J. M., et al. 2022, *MNRAS*, 512, 3464
 Wilde, J. W. 2023, PhD thesis, The Open University
 Zhang, T.-J. 2004, *ApJ*, 602, L5
 Zitrin, A., Rosati, P., Nonino, M., et al. 2012, *ApJ*, 749, 97

¹ Kapteyn Astronomical Institute, University of Groningen, PO Box 800, 9700 AV Groningen, The Netherlands

² Minnesota Institute for Astrophysics, University of Minnesota, 116 Church St SE, Minneapolis, MN 55455, USA

³ Institute of Physics, Laboratory of Astrophysics, Ecole Polytechnique Fédérale de Lausanne (EPFL), Observatoire de Sauverny, 1290 Versoix, Switzerland

⁴ Institut de Ciències del Cosmos (ICCUB), Universitat de Barcelona (IEEC-UB), Martí i Franquès 1, 08028 Barcelona, Spain

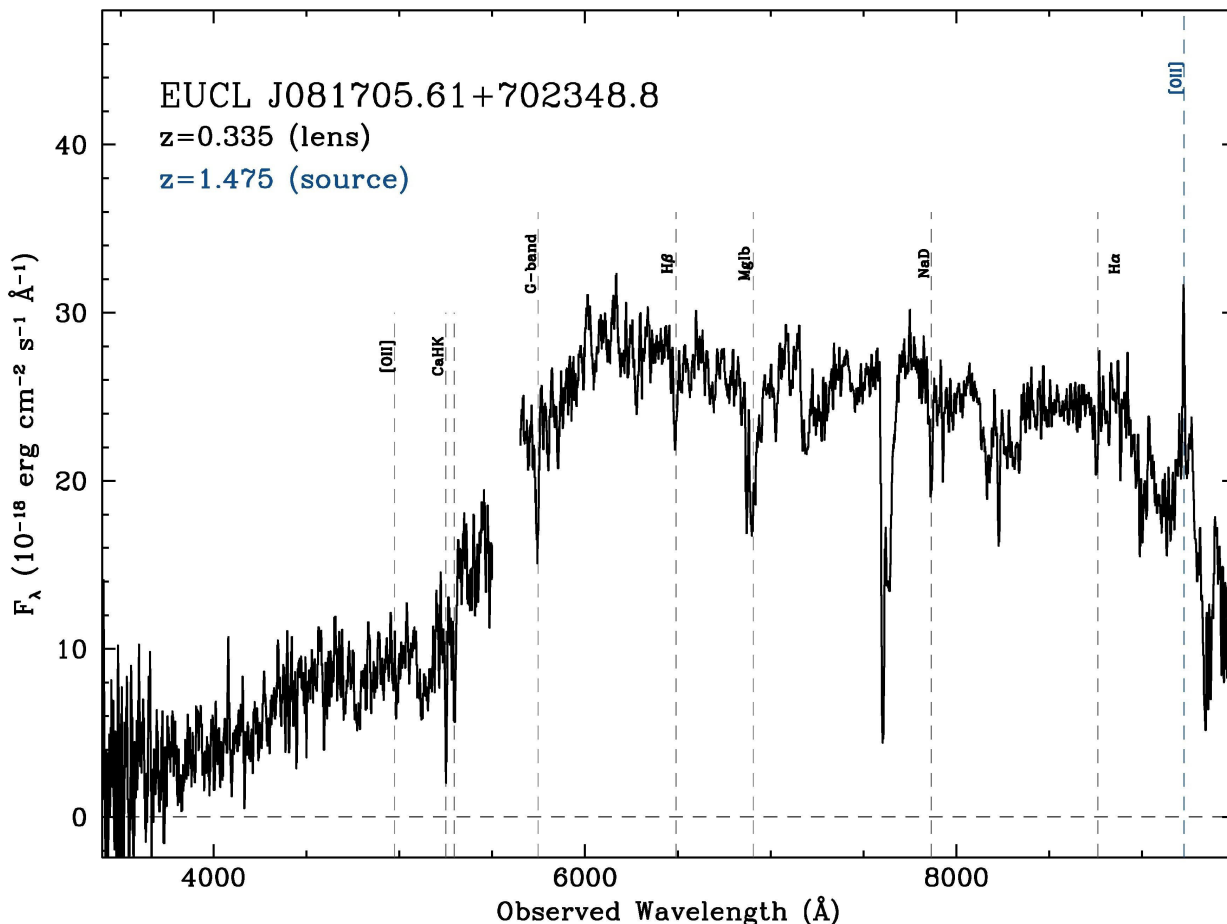


Fig. 6. Spectrum of the grade A strong lens candidate EUCL J081705.61+702348.8 obtained at Palomar Observatory. The spectrum reveals an early-type galaxy at $z = 0.335$ with several characteristic absorption lines in addition to a strong 4000 Å break. There is a strong additional line at 9222.8 Å, which we associate with [O II] emission from the lensed source galaxy at $z = 1.475$.

⁵ Technical University of Munich, TUM School of Natural Sciences, Physics Department, James-Frank-Str. 1, 85748 Garching, Germany

⁶ Max-Planck-Institut für Astrophysik, Karl-Schwarzschild-Str. 1, 85748 Garching, Germany

⁷ Departamento Física Aplicada, Universidad Politécnica de Cartagena, Campus Muralla del Mar, 30202 Cartagena, Murcia, Spain

⁸ School of Physical Sciences, The Open University, Milton Keynes, MK7 6AA, UK

⁹ Jet Propulsion Laboratory, California Institute of Technology, 4800 Oak Grove Drive, Pasadena, CA, 91109, USA

¹⁰ School of Mathematics, Statistics and Physics, Newcastle University, Herschel Building, Newcastle-upon-Tyne, NE1 7RU, UK

¹¹ Green Bank Observatory, P.O. Box 2, Green Bank, WV 24944, USA

¹² Dipartimento di Fisica e Astronomia "Augusto Righi" - Alma Mater Studiorum Università di Bologna, via Piero Gobetti 93/2, 40129 Bologna, Italy

¹³ INAF-Osservatorio di Astrofisica e Scienza dello Spazio di Bologna, Via Piero Gobetti 93/3, 40129 Bologna, Italy

¹⁴ University of Applied Sciences and Arts of Northwestern Switzerland, School of Engineering, 5210 Windisch, Switzerland

¹⁵ Institute of Cosmology and Gravitation, University of Portsmouth, Portsmouth PO1 3FX, UK

¹⁶ David A. Dunlap Department of Astronomy & Astrophysics, University of Toronto, 50 St George Street, Toronto, Ontario M5S 3H4, Canada

¹⁷ Jodrell Bank Centre for Astrophysics, Department of Physics and Astronomy, University of Manchester, Oxford Road, Manchester M13 9PL, UK

¹⁸ SCITAS, Ecole Polytechnique Fédérale de Lausanne (EPFL), 1015 Lausanne, Switzerland

¹⁹ INAF-Osservatorio Astronomico di Capodimonte, Via Moiariello 16, 80131 Napoli, Italy

²⁰ Aix-Marseille Université, CNRS, CNES, LAM, Marseille, France

²¹ Institut d'Astrophysique de Paris, UMR 7095, CNRS, and Sorbonne Université, 98 bis boulevard Arago, 75014 Paris, France

²² Department of Physics "E. Pancini", University Federico II, Via Cinthia 6, 80126, Napoli, Italy

²³ INFN section of Naples, Via Cinthia 6, 80126, Napoli, Italy

²⁴ Dipartimento di Fisica "Aldo Pontremoli", Università degli Studi di Milano, Via Celoria 16, 20133 Milano, Italy

²⁵ INAF-IASF Milano, Via Alfonso Corti 12, 20133 Milano, Italy

²⁶ Institució Catalana de Recerca i Estudis Avançats (ICREA), Pas-seig de Lluís Companys 23, 08010 Barcelona, Spain

²⁷ Department of Physics and Astronomy, Lehman College of the CUNY, Bronx, NY 10468, USA

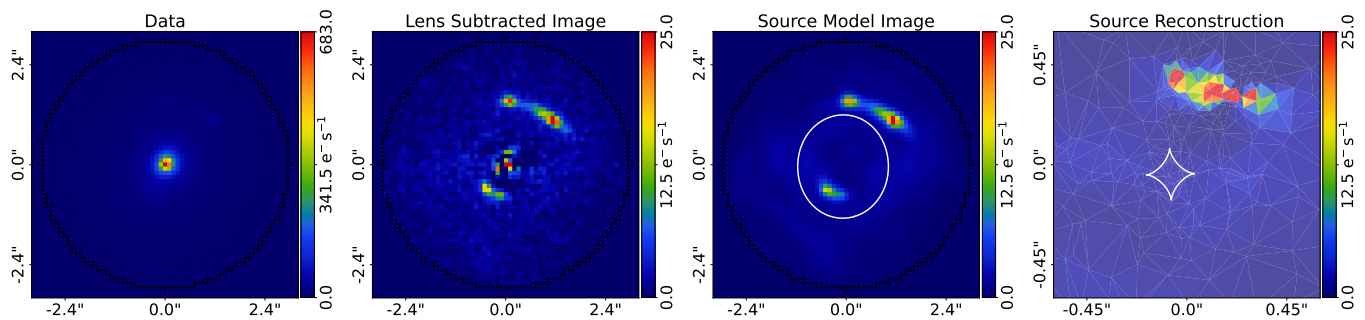


Fig. 7. Lens model of the grade A system EUCL J081705.61+702348.8, created using the *Euclid* strong lens modelling pipeline implemented with PyAutoLens (Nightingale et al. 2018, 2021). The panels show: (i) the observed VIS optical image; (ii) the lens-subtracted image; (iii) the lens model reconstruction of the lensed source; and (iv) the source galaxy’s reconstructed unlensed emission in the source plane. The system is accurately modelled, providing strong evidence of its lensing nature. The mass model is a singular isothermal ellipsoid with external shear, the lens light is modelled using a multi-Gaussian expansion (He et al. 2024), and the source is reconstructed on an adaptive Delaunay mesh. The inferred Einstein radius is $1'18 \pm 0'03$.

- 28 American Museum of Natural History, Department of Astrophysics, New York, NY 10024, USA
- 29 INFN-Sezione di Bologna, Viale Bertini Pichat 6/2, 40127 Bologna, Italy
- 30 Instituto de Física de Cantabria, Edificio Juan Jordá, Avenida de los Castros, 39005 Santander, Spain
- 31 Universitäts-Sternwarte München, Fakultät für Physik, Ludwig-Maximilians-Universität München, Scheinerstrasse 1, 81679 München, Germany
- 32 Max Planck Institute for Extraterrestrial Physics, Giessenbachstr. 1, 85748 Garching, Germany
- 33 National Astronomical Observatory of Japan, 2-21-1 Osawa, Mitaka, Tokyo 181-8588, Japan
- 34 Department of Physics & Astronomy, University of California Irvine, Irvine CA 92697, USA
- 35 UCB Lyon 1, CNRS/IN2P3, IUF, IP2I Lyon, 4 rue Enrico Fermi, 69622 Villeurbanne, France
- 36 STAR Institute, Quartier Agora - Allée du six Août, 19c B-4000 Liège, Belgium
- 37 University of Trento, Via Sommarive 14, I-38123 Trento, Italy
- 38 Dipartimento di Fisica e Astronomia, Università di Firenze, via G. Sansone 1, 50019 Sesto Fiorentino, Firenze, Italy
- 39 INAF-Osservatorio Astrofisico di Arcetri, Largo E. Fermi 5, 50125, Firenze, Italy
- 40 ESAC/ESA, Camino Bajo del Castillo, s/n., Urb. Villafranca del Castillo, 28692 Villanueva de la Cañada, Madrid, Spain
- 41 School of Mathematics and Physics, University of Surrey, Guildford, Surrey, GU2 7XH, UK
- 42 INAF-Osservatorio Astronomico di Brera, Via Brera 28, 20122 Milano, Italy
- 43 Université Paris-Saclay, Université Paris Cité, CEA, CNRS, AIM, 91191, Gif-sur-Yvette, France
- 44 IFPU, Institute for Fundamental Physics of the Universe, via Beirut 2, 34151 Trieste, Italy
- 45 INAF-Osservatorio Astronomico di Trieste, Via G. B. Tiepolo 11, 34143 Trieste, Italy
- 46 INFN, Sezione di Trieste, Via Valerio 2, 34127 Trieste TS, Italy
- 47 SISSA, International School for Advanced Studies, Via Bonomea 265, 34136 Trieste TS, Italy
- 48 Dipartimento di Fisica e Astronomia, Università di Bologna, Via Gobetti 93/2, 40129 Bologna, Italy
- 49 INAF-Osservatorio Astronomico di Padova, Via dell’Osservatorio 5, 35122 Padova, Italy
- 50 INAF-Osservatorio Astrofisico di Torino, Via Osservatorio 20, 10025 Pino Torinese (TO), Italy
- 51 Dipartimento di Fisica, Università di Genova, Via Dodecaneso 33, 16146, Genova, Italy
- 52 INFN-Sezione di Genova, Via Dodecaneso 33, 16146, Genova, Italy
- 53 Instituto de Astrofísica e Ciências do Espaço, Universidade do Porto, CAUP, Rua das Estrelas, PT4150-762 Porto, Portugal
- 54 Faculdade de Ciências da Universidade do Porto, Rua do Campo de Alegre, 4150-007 Porto, Portugal
- 55 Dipartimento di Fisica, Università degli Studi di Torino, Via P. Giuria 1, 10125 Torino, Italy
- 56 INFN-Sezione di Torino, Via P. Giuria 1, 10125 Torino, Italy
- 57 Centro de Investigaciones Energéticas, Medioambientales y Tecnológicas (CIEMAT), Avenida Complutense 40, 28040 Madrid, Spain
- 58 Port d’Informació Científica, Campus UAB, C. Albareda s/n, 08193 Bellaterra (Barcelona), Spain
- 59 Institute for Theoretical Particle Physics and Cosmology (TTK), RWTH Aachen University, 52056 Aachen, Germany
- 60 INAF-Osservatorio Astronomico di Roma, Via Frascati 33, 00078 Monteporzio Catone, Italy
- 61 Dipartimento di Fisica e Astronomia "Augusto Righi" - Alma Mater Studiorum Università di Bologna, Viale Bertini Pichat 6/2, 40127 Bologna, Italy
- 62 Instituto de Astrofísica de Canarias, Vía Láctea, 38205 La Laguna, Tenerife, Spain
- 63 Institute for Astronomy, University of Edinburgh, Royal Observatory, Blackford Hill, Edinburgh EH9 3HJ, UK
- 64 European Space Agency/ESRIN, Largo Galileo Galilei 1, 00044 Frascati, Roma, Italy
- 65 Université Claude Bernard Lyon 1, CNRS/IN2P3, IP2I Lyon, UMR 5822, Villeurbanne, F-69100, France
- 66 Mullard Space Science Laboratory, University College London, Holmbury St Mary, Dorking, Surrey RH5 6NT, UK
- 67 Departamento de Física, Faculdade de Ciências, Universidade de Lisboa, Edifício C8, Campo Grande, PT1749-016 Lisboa, Portugal
- 68 Instituto de Astrofísica e Ciências do Espaço, Faculdade de Ciências, Universidade de Lisboa, Campo Grande, 1749-016 Lisboa, Portugal
- 69 Department of Astronomy, University of Geneva, ch. d’Ecogia 16, 1290 Versoix, Switzerland
- 70 INAF-Istituto di Astrofisica e Planetologia Spaziali, via del Fosso del Cavaliere, 100, 00100 Roma, Italy
- 71 INFN-Padova, Via Marzolo 8, 35131 Padova, Italy
- 72 Aix-Marseille Université, CNRS/IN2P3, CPPM, Marseille, France
- 73 FRACTAL S.L.N.E., calle Tulipán 2, Portal 13 1A, 28231, Las Rozas de Madrid, Spain
- 74 Institute of Theoretical Astrophysics, University of Oslo, P.O. Box 1029 Blindern, 0315 Oslo, Norway
- 75 Department of Physics, Lancaster University, Lancaster, LA1 4YB, UK
- 76 Felix Hormuth Engineering, Goethestr. 17, 69181 Leimen, Germany
- 77 Technical University of Denmark, Elektrovej 327, 2800 Kgs. Lyngby, Denmark

- ⁷⁸ Cosmic Dawn Center (DAWN), Denmark
- ⁷⁹ Max-Planck-Institut für Astronomie, Königstuhl 17, 69117 Heidelberg, Germany
- ⁸⁰ NASA Goddard Space Flight Center, Greenbelt, MD 20771, USA
- ⁸¹ Department of Physics and Astronomy, University College London, Gower Street, London WC1E 6BT, UK
- ⁸² Department of Physics and Helsinki Institute of Physics, Gustaf Hällströmin katu 2, 00014 University of Helsinki, Finland
- ⁸³ Leiden Observatory, Leiden University, Einsteinweg 55, 2333 CC Leiden, The Netherlands
- ⁸⁴ Université de Genève, Département de Physique Théorique and Centre for Astroparticle Physics, 24 quai Ernest-Ansermet, CH-1211 Genève 4, Switzerland
- ⁸⁵ Department of Physics, P.O. Box 64, 00014 University of Helsinki, Finland
- ⁸⁶ Helsinki Institute of Physics, Gustaf Hällströmin katu 2, University of Helsinki, Helsinki, Finland
- ⁸⁷ European Space Agency/ESTEC, Keplerlaan 1, 2201 AZ Noordwijk, The Netherlands
- ⁸⁸ NOVA optical infrared instrumentation group at ASTRON, Oude Hoogeveensedijk 4, 7991PD, Dwingeloo, The Netherlands
- ⁸⁹ Centre de Calcul de l'IN2P3/CNRS, 21 avenue Pierre de Coubertin 69627 Villeurbanne Cedex, France
- ⁹⁰ Universität Bonn, Argelander-Institut für Astronomie, Auf dem Hügel 71, 53121 Bonn, Germany
- ⁹¹ INFN-Sezione di Roma, Piazzale Aldo Moro, 2 - c/o Dipartimento di Fisica, Edificio G. Marconi, 00185 Roma, Italy
- ⁹² Department of Physics, Institute for Computational Cosmology, Durham University, South Road, Durham, DH1 3LE, UK
- ⁹³ Institut d'Astrophysique de Paris, 98bis Boulevard Arago, 75014, Paris, France
- ⁹⁴ Institut de Física d'Altes Energies (IFAE), The Barcelona Institute of Science and Technology, Campus UAB, 08193 Bellaterra (Barcelona), Spain
- ⁹⁵ DARK, Niels Bohr Institute, University of Copenhagen, Jagtvej 155, 2200 Copenhagen, Denmark
- ⁹⁶ Waterloo Centre for Astrophysics, University of Waterloo, Waterloo, Ontario N2L 3G1, Canada
- ⁹⁷ Department of Physics and Astronomy, University of Waterloo, Waterloo, Ontario N2L 3G1, Canada
- ⁹⁸ Perimeter Institute for Theoretical Physics, Waterloo, Ontario N2L 2Y5, Canada
- ⁹⁹ Space Science Data Center, Italian Space Agency, via del Politecnico snc, 00133 Roma, Italy
- ¹⁰⁰ Centre National d'Etudes Spatiales – Centre spatial de Toulouse, 18 avenue Edouard Belin, 31401 Toulouse Cedex 9, France
- ¹⁰¹ Institute of Space Science, Str. Atomistilor, nr. 409 Măgurele, Ilfov, 077125, Romania
- ¹⁰² Consejo Superior de Investigaciones Científicas, Calle Serrano 117, 28006 Madrid, Spain
- ¹⁰³ Universidad de La Laguna, Departamento de Astrofísica, 38206 La Laguna, Tenerife, Spain
- ¹⁰⁴ Dipartimento di Fisica e Astronomia "G. Galilei", Università di Padova, Via Marzolo 8, 35131 Padova, Italy
- ¹⁰⁵ Institut für Theoretische Physik, University of Heidelberg, Philosophenweg 16, 69120 Heidelberg, Germany
- ¹⁰⁶ Institut de Recherche en Astrophysique et Planétologie (IRAP), Université de Toulouse, CNRS, UPS, CNES, 14 Av. Edouard Belin, 31400 Toulouse, France
- ¹⁰⁷ Université St Joseph; Faculty of Sciences, Beirut, Lebanon
- ¹⁰⁸ Departamento de Física, FCFM, Universidad de Chile, Blanco Encalada 2008, Santiago, Chile
- ¹⁰⁹ Universität Innsbruck, Institut für Astro- und Teilchenphysik, Technikerstr. 25/8, 6020 Innsbruck, Austria
- ¹¹⁰ Institut d'Estudis Espacials de Catalunya (IEEC), Edifici RDIT, Campus UPC, 08860 Castelldefels, Barcelona, Spain
- ¹¹¹ Satlantis, University Science Park, Sede Bld 48940, Leioa-Bilbao, Spain
- ¹¹² Institute of Space Sciences (ICE, CSIC), Campus UAB, Carrer de Can Magrans, s/n, 08193 Barcelona, Spain
- ¹¹³ Centre for Electronic Imaging, Open University, Walton Hall, Milton Keynes, MK7 6AA, UK
- ¹¹⁴ Infrared Processing and Analysis Center, California Institute of Technology, Pasadena, CA 91125, USA
- ¹¹⁵ Instituto de Astrofísica e Ciências do Espaço, Faculdade de Ciências, Universidade de Lisboa, Tapada da Ajuda, 1349-018 Lisboa, Portugal
- ¹¹⁶ Universidad Politécnica de Cartagena, Departamento de Electrónica y Tecnología de Computadoras, Plaza del Hospital 1, 30202 Cartagena, Spain
- ¹¹⁷ Centre for Information Technology, University of Groningen, P.O. Box 11044, 9700 CA Groningen, The Netherlands
- ¹¹⁸ INFN-Bologna, Via Irnerio 46, 40126 Bologna, Italy
- ¹¹⁹ INAF, Istituto di Radioastronomia, Via Piero Gobetti 101, 40129 Bologna, Italy
- ¹²⁰ Aurora Technology for European Space Agency (ESA), Camino bajo del Castillo, s/n, Urbanización Villafranca del Castillo, Villanueva de la Cañada, 28692 Madrid, Spain
- ¹²¹ ICL, Junia, Université Catholique de Lille, LITL, 59000 Lille, France

Appendix A: Lens candidates

We show the details of 97 lens candidates which are distributed as 14 grade A candidates, 31 grade B candidates, and 52 grade C candidates.

Table A.1. Probable lens candidates discovered with CNN classifiers. ID, IAU Name, Fields, RA, DEC, Classification prediction scores for five different networks (P1, P2, P3, P4 and P5), Geometric Mean (GM) of the five prediction scores and visual inspection grade are shown. Here, P1 refers to the Lens-CLR network, P2 refers to the DenseLens, P3 refers to the 4-Layer CNN, P4 refers to the Naberrrie and P5 refers to the MRC95.

IAU Name	Field	RA	Dec	P1	P2	P3	P4	P5	GM	Grade
EUCL J215447.40+174003.7	Abell 2390	328.697535	17.667696	0.990	0.880	0.936	0.006	0.999	0.353	A
EUCL J215405.95+181205.2	Abell 2390	328.524807	18.201453	0.966	0.999	0.974	0.704	0.998	0.920	A
EUCL J002251.41-494843.9	Abell 2764	5.714233	-49.812211	0.211	0.470	0.998	0.093	0.999	0.392	A
EUCL J002539.83-491515.5	Abell 2764	6.415961	-49.254323	0.982	0.817	0.822	0.172	0.999	0.647	A
EUCL J002330.90-485506.4	Abell 2764	5.878780	-48.918448	0.972	0.980	0.982	0.503	0.999	0.860	A
EUCL J053110.94+121542.8	Barnard 30	82.795595	12.261915	0.750	0.014	0.989	0.854	0.786	0.373	A
EUCL J041819.40-554659.7	Dorado	64.580860	-55.783276	0.981	0.693	0.881	0.382	1.000	0.744	A
EUCL J041729.09-554120.0	Dorado	64.371238	-55.688895	0.889	0.572	1.000	0.471	1.000	0.751	A
EUCL J033706.49-351842.4	Fornax	54.277074	-35.311798	0.767	0.235	0.999	0.315	0.999	0.563	A
EUCL J033646.89-351138.8	Fornax	54.195391	-35.194112	0.994	0.995	0.991	0.014	0.999	0.428	A
EUCL J081945.02+702002.2	Holmberg II	124.937617	70.333964	0.024	0.432	0.422	0.008	0.999	0.131	A
EUCL J081705.61+702348.8	Holmberg II	124.273402	70.396896	0.930	0.946	0.992	0.891	0.999	0.951	A
EUCL J002035.05+585556.2	IC 10	5.146066	58.932298	0.131	0.801	0.858	0.763	0.999	0.585	A
EUCL J191245.11-634926.2	NGC 6744	288.187969	-63.823954	0.413	0.738	0.864	0.901	0.999	0.750	A
EUCL J215439.38+173354.6	Abell 2390	328.664120	17.565190	0.950	0.130	0.999	0.177	0.999	0.465	B
EUCL J215354.10+175419.0	Abell 2390	328.475438	17.905296	0.931	0.236	0.987	0.928	0.826	0.698	B
EUCL J215252.97+171932.8	Abell 2390	328.220730	17.325797	0.977	0.691	0.997	0.862	0.508	0.783	B
EUCL J002136.55-492944.5	Abell 2764	5.402328	-49.495699	0.993	0.917	0.791	0.097	0.940	0.581	B
EUCL J002313.02-492640.7	Abell 2764	5.804288	-49.444665	0.959	0.927	0.998	0.215	0.999	0.718	B
EUCL J002352.59-492403.3	Abell 2764	5.969141	-49.400920	0.104	0.735	0.999	0.073	0.999	0.354	B
EUCL J002255.86-492228.2	Abell 2764	5.732785	-49.374505	0.019	0.535	0.800	0.576	0.999	0.342	B
EUCL J002304.81-491845.7	Abell 2764	5.770044	-49.312716	0.689	0.474	0.494	0.511	0.996	0.607	B
EUCL J002442.16-491345.8	Abell 2764	6.175704	-49.229391	0.941	0.738	0.121	0.637	0.931	0.549	B
EUCL J002148.37-490541.5	Abell 2764	5.451552	-49.094878	0.996	0.798	0.999	0.386	0.999	0.789	B
EUCL J002131.51-490533.6	Abell 2764	5.381318	-49.092670	0.892	0.483	0.998	0.774	0.111	0.517	B
EUCL J002133.06-490020.3	Abell 2764	5.387787	-49.005661	0.329	0.464	0.999	0.050	0.999	0.377	B
EUCL J041425.56-555929.9	Dorado	63.606523	-55.991655	0.993	0.216	1.000	0.894	0.999	0.719	B
EUCL J041841.96-555503.4	Dorado	64.674870	-55.917617	0.962	0.068	0.519	0.909	0.816	0.517	B
EUCL J041556.54-555447.6	Dorado	63.985615	-55.913242	0.912	0.468	0.997	0.845	0.886	0.796	B
EUCL J041629.29-553257.7	Dorado	64.122045	-55.549366	0.894	0.974	0.999	0.804	0.635	0.850	B
EUCL J041335.15-552856.9	Dorado	63.396468	-55.482498	0.999	0.422	0.863	0.827	0.955	0.779	B
EUCL J081943.34+702335.6	Holmberg II	124.930595	70.393246	0.345	0.293	0.998	0.785	0.999	0.602	B
EUCL J081959.64+710219.7	Holmberg II	124.998533	71.038816	0.755	0.493	1.000	0.074	0.999	0.487	B
EUCL J001727.46+591801.9	IC 10	4.364447	59.300532	0.400	0.339	0.948	0.898	0.997	0.649	B
EUCL J054527.40-000548.7	Messier 78	86.364175	-0.096864	0.232	0.355	0.463	0.785	0.001	0.124	B
EUCL J054807.82+001045.5	Messier 78	87.032612	0.179325	0.759	0.352	0.059	0.071	0.999	0.258	B
EUCL J074006.13+655047.9	NGC 2403	115.025578	65.846644	0.574	0.304	0.303	0.917	0.996	0.546	B
EUCL J073450.92+655829.7	NGC 2403	113.712202	65.974936	0.246	0.104	0.562	0.885	0.999	0.418	B
EUCL J073851.49+655650.2	NGC 2403	114.714583	65.947284	0.992	0.723	0.977	0.560	0.949	0.821	B
EUCL J073637.17+660131.1	NGC 2403	114.154879	66.025315	0.556	0.157	0.996	0.754	0.692	0.539	B
EUCL J073600.54+651440.8	NGC 2403	114.002254	65.244693	0.985	0.612	0.999	0.728	0.788	0.809	B
EUCL J073924.78+651814.3	NGC 2403	114.853255	65.303999	0.766	0.367	0.580	0.051	0.999	0.384	B
EUCL J073609.14+651905.3	NGC 2403	114.038123	65.318153	0.702	0.925	0.999	0.463	0.742	0.741	B
EUCL J073910.33+652326.4	NGC 2403	114.793076	65.390688	0.982	0.759	0.999	0.254	0.999	0.717	B
EUCL J190644.53-635426.5	NGC 6744	286.685558	-63.907383	0.169	0.511	0.998	0.009	0.999	0.241	B
EUCL J215221.29+172946.7	Abell 2390	328.088745	17.496325	0.872	0.404	0.987	0.104	0.999	0.515	C
EUCL J215513.19+173144.9	Abell 2390	328.804966	17.529147	0.344	0.392	0.900	0.392	0.999	0.544	C
EUCL J215340.38+173401.9	Abell 2390	328.418271	17.567201	0.564	0.673	0.943	0.770	0.999	0.773	C
EUCL J215209.01+173724.4	Abell 2390	328.037552	17.623459	0.319	0.316	0.895	0.271	0.999	0.476	C
EUCL J215433.25+173935.1	Abell 2390	328.638549	17.659777	0.984	0.137	0.304	0.952	0.999	0.522	C
EUCL J215318.13+170941.8	Abell 2390	328.325546	17.161622	0.970	0.298	0.956	0.406	0.866	0.627	C
EUCL J215408.45+171749.6	Abell 2390	328.535221	17.297134	0.984	0.091	0.403	0.949	0.999	0.509	C
EUCL J215408.83+171841.1	Abell 2390	328.536832	17.311437	0.002	0.327	0.162	0.880	0.999	0.165	C
EUCL J215221.33+175326.5	Abell 2390	328.088883	17.890708	0.976	0.723	0.847	0.525	0.999	0.793	C
EUCL J215434.03+175344.6	Abell 2390	328.641815	17.895743	0.962	0.085	0.997	0.944	0.999	0.598	C

EUCL J215402.36+175523.2	Abell 2390	328.509837	17.923113	0.776	0.699	0.985	0.849	0.999	0.854	C
EUCL J215414.92+175605.7	Abell 2390	328.562193	17.934936	0.929	0.834	0.990	0.172	0.999	0.667	C
EUCL J215330.43+180324.0	Abell 2390	328.376812	18.056668	0.925	0.069	0.985	0.919	0.999	0.566	C
EUCL J215317.98+172027.6	Abell 2390	328.324921	17.341027	0.835	0.758	0.997	0.903	0.774	0.849	C
EUCL J002220.97-494451.2	Abell 2764	5.587376	-49.747565	0.154	0.553	0.999	0.023	0.999	0.288	C
EUCL J002320.05-492820.9	Abell 2764	5.833578	-49.472500	0.977	0.126	0.981	0.802	0.999	0.627	C
EUCL J002409.51-492435.5	Abell 2764	6.039630	-49.409882	0.964	0.519	0.999	0.415	0.999	0.730	C
EUCL J002542.83-491711.4	Abell 2764	6.428471	-49.286524	0.701	0.178	0.943	0.504	0.999	0.568	C
EUCL J002448.83-491148.7	Abell 2764	6.203498	-49.196888	0.225	0.907	0.999	0.145	0.999	0.495	C
EUCL J002121.46-490818.2	Abell 2764	5.339445	-49.138403	0.943	0.407	0.818	0.798	0.999	0.758	C
EUCL J002146.64-490317.1	Abell 2764	5.444347	-49.054750	0.646	0.653	0.999	0.066	0.999	0.489	C
EUCL J002058.08-490059.3	Abell 2764	5.242019	-49.016492	0.979	0.057	0.674	0.909	0.999	0.510	C
EUCL J002340.88-485337.0	Abell 2764	5.920356	-48.893632	0.422	0.643	0.991	0.156	0.999	0.530	C
EUCL J002359.71-493511.5	Abell 2764	5.998816	-49.586542	0.882	0.325	0.999	0.112	0.999	0.503	C
EUCL J002409.93-493232.6	Abell 2764	6.041410	-49.542403	0.960	0.690	0.999	0.832	0.998	0.887	C
EUCL J002130.78-493227.7	Abell 2764	5.378283	-49.541048	0.987	0.362	0.280	0.687	0.786	0.558	C
EUCL J053138.19+115948.7	Barnard 30	82.909158	11.996874	0.917	0.253	0.606	0.914	0.913	0.651	C
EUCL J041709.25-555512.4	Dorado	64.288546	-55.920135	0.955	0.002	0.946	0.922	1.000	0.608	C
EUCL J041356.98-553653.0	Dorado	63.487439	-55.614728	0.553	0.523	0.995	0.886	1.000	0.761	C
EUCL J041851.12-553221.9	Dorado	64.713024	-55.539426	0.597	0.039	0.991	0.401	0.788	0.451	C
EUCL J041644.82-552500.1	Dorado	64.186769	-55.416712	0.927	0.260	0.863	0.622	0.565	0.593	C
EUCL J041529.20-560110.6	Dorado	63.871674	-56.019634	0.958	0.759	0.872	0.213	0.996	0.670	C
EUCL J033701.08-353733.9	Fornax	54.254540	-35.626088	0.411	0.485	0.998	0.061	0.999	0.414	C
EUCL J033623.94-351003.0	Fornax	54.099781	-35.167520	0.887	0.194	0.259	0.496	0.995	0.466	C
EUCL J033526.99-350049.6	Fornax	53.862486	-35.013784	0.638	0.146	0.156	0.297	0.999	0.336	C
EUCL J082043.26+703648.3	Holmberg II	125.180250	70.613437	0.994	0.394	0.849	0.807	0.999	0.769	C
EUCL J082047.39+703833.6	Holmberg II	125.197494	70.642678	0.555	0.837	0.999	0.233	0.999	0.641	C
EUCL J081627.48+702225.2	Holmberg II	124.114541	70.373679	0.920	0.652	0.998	0.919	0.982	0.884	C
EUCL J081755.78+704950.4	Holmberg II	124.482442	70.830679	0.912	0.027	0.999	0.532	0.999	0.420	C
EUCL J081846.26+705231.7	Holmberg II	124.692781	70.875493	0.971	0.650	0.998	0.267	0.998	0.700	C
EUCL J082139.67+710505.6	Holmberg II	125.415301	71.084913	0.618	0.274	0.997	0.164	0.999	0.488	C
EUCL J081648.17+702703.3	Holmberg II	124.200716	70.450925	0.981	0.349	0.771	0.155	0.995	0.527	C
EUCL J002142.42+591721.0	IC 10	5.426777	59.289174	0.720	0.163	0.993	0.886	0.999	0.635	C
EUCL J073800.72+654951.2	NGC 2403	114.503007	65.830916	0.906	0.668	0.995	0.242	0.999	0.680	C
EUCL J073708.65+655559.7	NGC 2403	114.286066	65.933256	0.790	0.092	0.482	0.572	0.999	0.458	C
EUCL J074015.20+652735.0	NGC 2403	115.063350	65.459746	0.238	0.929	0.999	0.354	0.998	0.601	C
EUCL J073439.30+654117.1	NGC 2403	113.663751	65.688102	0.081	0.898	0.943	0.013	0.999	0.248	C
EUCL J174240.46-535547.7	NGC 6397	265.668618	-53.929936	0.440	0.298	0.743	0.929	0.999	0.618	C
EUCL J194516.93-143333.9	NGC 6822	296.320580	-14.559422	0.972	0.027	1.000	0.078	0.999	0.376	C
EUCL J194325.36-142833.9	NGC 6822	295.855690	-14.476105	0.323	0.294	0.779	0.506	1.000	0.518	C
EUCL J194458.53-150442.9	NGC 6822	296.243914	-15.078600	0.730	0.094	0.845	0.918	1.000	0.563	C
EUCL J041956.87+275802.6	Taurus	64.986995	27.967397	0.650	0.506	0.609	0.302	0.997	0.570	C

Appendix B: Summary of the ERO fields

We present here the summary of the 16 *Euclid* ERO fields (except Perseus). The *Euclid* VIS instrument provides high-quality optical imaging through a single broad optical band (550–900 nm). The VIS camera features a pixel scale of $0''.1$ per pixel. The point spread function (PSF) of VIS has a full width at half maximum (FWHM) of $\lesssim 0''.18$ across the entire field of view (Cropper et al. 2016). For the ERO fields, each pointing consists of four dithered exposures of 565 seconds each, resulting in a total exposure time of 2260 seconds. This yields a typical 5σ point-source depth of $I_E \approx 26.2$ mag (Euclid Collaboration: Scaramella et al. 2022). The VIS images demonstrate excellent depth and resolution, with a median signal-to-noise ratio (S/N) of $\sim 10\sigma$ for objects at $I_E = 24.5$ mag.

Table B.1. Summary of all the 16 *Euclid* ERO Fields (except Perseus) including their corresponding area, and their corresponding catalogue size, which represents the number of sources in each field.

Field name	Area (deg ²)	Catalogue size
Abell 2390	0.75	469 056
Abell 2764	0.75	542 729
Barnard 30	0.6	163 063
Dorado	0.6	518 445
Fornax	0.57	369 315
Holmberg II	0.6	466 276
Horsehead Nebula	0.58	157 264
IC 10	0.62	1 403 807
IC 342	0.59	2 033 293
M78	0.6	116 373
NGC 2403	0.6	1 152 966
NGC 6254	0.6	413 297
NGC 6397	0.61	782 612
NGC 6744	0.6	924 913
NGC 6822	0.6	1 694 021
Taurus	0.61	123 726